Revealing the Effects of the Non-Solvent on the Ligand Shell of Nanoparticles and Their Crystallization

Byeongdu Lee,[≠*] *Kenneth Littrell,*[∓] *Yuchen Sha,*[‡⊥] *and Elena V. Shevchenko*[‡*]

[*≠]Advanced Photon Source, Argonne National Laboratory, Argonne, Illinois 60439 USA;

[∓] Neutron Sciences Directorate, Oak Ridge National Laboratory, Oak Ridge, TN 37831;

[⊥] Institute of Advanced Studies (IAS), College of Chemistry and Molecular Sciences, Wuhan University, Wuhan 430072, Hubei, P. R. China;

[‡]Center for Nanoscale Materials, Argonne National Laboratory, Argonne, Illinois 60439 USA;

KEYWORDS. Reciprocal space mapping, SAXS, self-assembly, supercrystal, nanoparticles, solvent ligand interaction, and colloidal solution destabilization.

ABSTRACT

When nanoparticles (NPs) are assembled from solution, a common assembly method of choice is either solution destabilization or solvent evaporation technique. The destabilization of the NP solution by non-solvents results in the formation of faceted supercrystals (SCs) while periodic film-like assemblies are typically formed by solvent evaporation. Here, we reveal the effect of non-solvents in washing, dispersing, and crystallizing NPs. Small angle neutron scattering (SANS) is employed for monitoring the ligand shell of NPs in solutions upon introduction of various non-solvents. The SC crystallization process is traced in-situ with small angle x-ray scattering (SAXS), and structures of resulted single crystalline SCs are examined in detail by mapping the reciprocal space using SAXS and wide-angle x-ray scattering. Our study suggests that the relative miscibility of the non-solvent with solvents and ligands determines the solvation and thickness of the ligand shell and thereby the resulting structure of SCs. In the early stage of crystallization, truncated octahedral PbS NPs form SCs with face centered cubic (fcc) symmetry. In the later stage, the fcc symmetry is preseved in the SC formed by larger (5.60 nm) NPs, but the SC assembled from smaller (4.14 nm) NPs undergoes a phase transition into body centered cubic (bcc) lattice via Bain transformation, becoming a polycrystalline SC containing three structurally-correlated bcc domains and one untransformed fcc domain. Our study provides the detailed understanding of the non-solvent effect that impacts beyond the formation of SCs, enabling the judicious selection of solvent/non-solvent mixtures for NP purification.

Introduction

Surface molecules (ligands) attached to the surface of nanoparticles (NPs)[1-3] provide colloidal stability and determine the solubility of NPs in a given solvent. Dispersion of NPs in solution is a prerequisite step toward assembly of NPs into new, customized materials,[4] which have been of a great interest for their applications in the design of field effect transistors, lasers, detectors, etc.[5] The assembly of NPs from a solution is a complex process requiring a delicate control over the interactions between neighboring particles in solution,[6-7] which are mainly governed by ligands.

In solution, surface ligands interface two incompatible materials, such as solid inorganic core and the solvent. The NPs synthesized in a polar solvent (e.g. aqueous solution) are electrostatically stabilized against their aggregation by a charged bilayer.[8-9] In the case of NPs synthesized in organic solution, ligand molecules form a monolayer on the NP surface with their hydrocarbon ends facing the nonpolar medium.[10-11] Good dispersion both in polar and nonpolar solvents implies that the ligand shells enable NPs in solution to be repulsive to each other or at least neutral. For formation of long-range ordered periodic structures, it is important to keep the net interparticle interactions weakly attractive so that NPs can assemble and dynamically reorganize into ideal coordination configuration during assembly.[12] In polar solvents, this is achieved by controlling NP charges, requiring sophisticated engineering of the surface molecules.[2, 8, 13-16] On the other hand, in nonpolar solvents NP assemblies can be formed by increasing NP concentration through solvent evaporation [17-20] or by controllable oversaturation of the colloidal solution with non-solvent, called the destabilization method.[21-23] Solvent evaporation typically enables the fabrication of continuous, long-range periodic films, while the solution destabilization method [24-25] results in the growth of three-dimensional NP supercrystals (SCs) that adopt shapes similar to those of inorganic crystals formed by atoms. [23, 26]

A rather good understanding has been gained by studying NP assembly induced by solvent evaporation.[27] Diverse packing structures of NPs have been reported for assemblies deposited from nonpolar solution.[4, 7, 28] Generally, NPs tend to assemble into the structure that maximizes the packing entropy, i.e. the densest packing structure,[7] dictating the orientations of individual NPs if they are not spherical.[29-30] Since the NPs are rarely hard non-interacting spheres, the structure is expected to maximize the pair-potential interactions between NPs, including dipole-dipole

interactions,[31] van-der-Waals interaction between inorganic NP cores,[32-33] and specific interactions between ligands.[34-36] These assemblies may interact with substrates, and such in-plane interaction may lead to distorted SC structures.[37-39] Recently, in spherical NP systems, attention has been focused on the conformational entropy of ligand chains as it has been observed that spherical NPs with smaller core sizes tend to assemble into a structure with a body-centered cubic (bcc) lattice while NPs with larger cores form a face-centered cubic (fcc) structure that is the highest-packing structure of hard spheres.[40-41] The bcc structure maximizes the conformational entropy of the ligands when they occupy a significant volume fraction of NP assemblies, which is a well-studied subject in soft matter, e.g. assemblies of micelles with long, tethered chains such as block copolymers.[42] The difference between the packing symmetries of the structures formed by smaller and larger NPs can be attributed to the fact that the surface area of the Voronoi-cell of the bcc lattice is smaller than that of the fcc lattice,[43] providing space for the chains to stretch out along the normal direction to the NP surface. As a result, the gain in the conformational entropy via the fcc to bcc transformation can be higher than the loss in the NP packing entropy.

The packing entropy of the lattice depends on the particle shape.[29] For example, for the truncated octahedra that are the Wigner-Seitz cells of the bcc lattice, the packing entropy of NPs and conformational entropy of surface ligands can cooperate to form NP SCs with bcc lattice.[39, 43] Indeed, truncated octahedral PbS NPs coated with oleic acids were reported to self-assemble into a bcc structure when their size is less than 5 nm.[23] However, when their size is larger than 5 nm, they form fcc structures,[44-45] compromising the conformational entropy gain and behaving like spheres, suggesting the "screening" of the NP shape by the surface ligands. The fcc packing structure from the truncated octahedral NPs is not the densest packing structure but only maximizes configuration entropy of NPs[39] and is thus less stable than the densest packing bcc structure.[46] The "screening" effect of the ligand shell can be eliminated by the partial ligand removal from the NP surface. [47-48] On the other hand, addition of ligands can alter the polyhedral-type packing into sphere-like particle packing. For example, in the presence of extra ligands, cubic gold NPs of which densest packing structure is simple cubic assemble into a rhombohedral structure that is basically a slightly distorted fcc structure.[49] As the size ratio between NP cores and thickness of ligand shells increases further, this screening effect becomes insignificant, driving the large NPs with short ligands to assemble again into bcc structures, as was observed for 7.3 nm PbS NPs.[50]

As recent studies demonstrate, the type of solvent also affects the assembly structure of ligand coated NPs.[27, 51-52] For example, PbS NPs passivated with oleic acids form fcc[51] and bcc[53] structures upon evaporation of hexane and toluene solutions, respectively. In hexane, the oleic acid shell is more solvated as compared to toluene, making the NPs more repulsive to each other.[54] These highly solvated, repulsive NPs behave as hard spheres, resulting in the formation of fcc structure as they become increasingly concentrated upon drying. However, recently Wang et al. reported PbS NPs in hexane formed only bcc structures while those in toluene formed both bcc and fcc structures as the solvent evaporated.[27] These conflicting results suggest that there is more to explore about the role of the solvents. In the solution destabilization method, the overall NP concentration in solution does not change with time. However, extending knowledge from polymer science,[55] we expect that the solvated repulsive NPs will become gradually less repulsive or even attractive as non-solvent mixes into the NP solution,[56] and that the conformation of grafted ligands adjust to the mixed-solvent environment.[57]

Periodic films formed by solvent evaporation and SCs formed by the destabilization method from the same NPs have a few important differences. Previously, we have found that SCs formed by 7.0 nm PbS NPs passivated with oleic acid molecules displayed a shorter interparticle spacing of ~1.4 nm[58] as compared to 1.9 - 2.7 nm spacing observed in long range periodic films obtained through solvent evaporation.[59] The interparticle spacings of SCs were found to increase with temperature without NP sintering up to 180 ^{o}C [58] as opposed to a decrease in spacing with increasing temperature observed in periodic films.[59] The origin of this smaller interparticle spacing in the SCs was partly attributed to the possible ligand removal by non-solvents[24, 58] by assuming fewer ligands in SCs formed by more polar non-solvents. However, this hypothesis has never been proved experimentally.

Here, we report on how solvent, non-solvent, and ligand molecules interact with each other, and how their interactions affect the self-assembly process and the final SC structures. We demonstrate that we can tune the interaction between ligands, interparticle spacing, and kinetics of assembly by choosing different non-solvents. By employing SAXS and SANS techniques, we were able to study structural details of SCs at various growth steps, revealing the mechanism of the destabilization of the colloidal solution by a non-solvent leading to the formation of faceted SCs. Our findings provide important insights into the solvent/non-solvent technique that is

commonly used to purify NPs. In addition, our study unifies the results obtained in studies on NP assembly by evaporation.

Experimental Section

Chemicals. Lead(II) oxide (99.999%), 1-octadecene (ODE, 90%), oleic acid (OA, 90%), hexamethyldisilthiane (TMS_2S), the solvents (methanol, ethanol, iso-propanol and hexane) of analytical grade were purchased from Aldrich. All chemicals were used as received.

Sample preparation for scattering experiments. The PbS NPs with smaller (3.96 and 4.14 nm) and larger (5.43 and 5.60 nm) core sizes were synthesized using a previously-reported approach.[23] Our study focuses on the analysis of the samples obtained using 4.14 and 5.60 nm PbS NPs. The different batches of PbS NPs presented slight size variations. Sizes of NPs used in heating and SANS experiments were slightly smaller, 3.96 nm and 5.43 nm, respectively, but we labeled them as 4.14 and 5.60 nm, respectively, in this work for better readability.

In assembly experiments, the synthesized PbS NPs were purified from the unreacted species and excess of the organic substances by addition of double the volume of the non-solvent (isopropanol) to the reaction mixture, followed by centrifugation at 4500 rpm for 5 min. The precipitate was re-dispersed first in hexane and then in toluene in the first and second purification cycles, respectively. After that, ~1 mL of the colloidal solution was placed into a crystallization test tube and 3 mL of non-solvents (methanol, ethanol and isopropanol) were added. Each crystallization tube contained a strip of glass substrate to serve as a crystallization center. The top of the test tubes was sealed with parafilm to prevent solvent evaporation. After 2 weeks, the test tubes were opened and the SCs were characterized.

In SANS experiments, the NPs were synthesized and purified the same way described above. After the purification, 41 mg of PbS NPs were re-dispersed in about 10 mL of hexane. A day before SANS sample preparation, the solvent was evaporated by blowing N_2. Then, 6.5 mL of toluene-d8 was added to the dried PbS NPs to make a stock solution. For each SANS sample, 0.5 mL of the stock solution was transferred to 2 mL vials and diluted to 1 mL using toluene-d8 and deuterated alcohols. The concentration of the deuterated alcohols was varied in a range between 5 and 40 vol %.

Small angle neutron scattering (SANS) SANS experiments were conducted at the CG2 General Purpose-SANS (GP_SANS) beamline of HFIR in Oak Ridge National Laboratory. Data were collected at three different sample-to-detector distances. The combined, total exposure time for the three q ranges was 1hr for each sample. PbS solutions in the mixed deuterated solvents were injected into quartz cuvette cell with thickness of 2 mm. Data processing including background subtraction and azimuthal averaging was done using the IGOR-based program provided by the beamline. Raw data and fitting results are available in the Supporting Information.

Small angle x-ray scattering (SAXS) and wide angle x-ray scattering (WAXS) SAXS and WAXS were collected at the 12-ID-B beamline of the Advanced Photon Source in the Argonne National Laboratory. SAXS and WAXS were simultaneously measured for solution samples in a flow-cell with a capillary of 1.5 mm diameter. For solution measurements, an X-ray beam with energy of 14 keV, or wavelength λ = 0.8856 Å, and size of 300 x 100 um^2 was used, with each sample typically exposed to the beam for one second. The detectors used for SAXS and WAXS were a Pilatus2M and a Pilatus300k, respectively. Absolute intensity was calculated using water as a standard.

For full SAXS and WAXS reciprocal spacing mapping measurements, data were collected with Pilatus2M and PerkinElmer XRPad 4343F detectors located at about 2 m and 180 mm, respectively. The scattering angle 2θ is converted to the scattering vector $q = 4\pi \sin\theta / \lambda$ using the silver behenate standard. The X-ray beam was focused on the sample with a spot size of 200 x 30 um^2. SAXS and WAXS data were corrected for background, flux variation, and polarization. SAXS data were additionally corrected for absorption, but WAXS were not because it was impractical to estimate the shape dependent angular absorption. Details of the mapping procedure are described in the Supporting Information.

For the heating experiments, SCs were deposited on thin glass coverslips. After completely drying in ambient condition for weeks, they were then mounted to a temperature controlled heater available at the 12-ID-B beamline. Samples were heated in air from room temperature to 225 ^oC with a ramping rate of 3 ^oC/min. X-ray exposure time was 0.1 seconds.

For in-situ SAXS experiment, toluene solutions of PbS NPs were injected into 1.5 mm diameter quartz capillary tubes, filling a quarter of the length of the tube. Immediately, a double volume of

the non-solvent was added to each tube, and the tubes were capped with parafilm. The tubes were then loaded to the capillary rack at the beamline, and the rack was mounted on the SAXS sample stage. Data were collected with an exposure time of 0.1 seconds at various positions along the tubes every 15 mins for two hours. After the measurements, the sample rack was carefully removed from the sample stage and stored at ambient condition to let the crystallization proceed. The samples were measured again at about 18 and 40 hours later.

Thermogravimetric Analysis (**TGA**) measurements were performed with a Mettler-Toledo STAR^e TGA/SDTA851^e system operated under inert, N_2 atmosphere. We used 5 ^{o}C/min ramping rate. The SCs samples (1.1 - 2.4 mg for each sample) were detached from the glass substrate and placed into Al boats.

Optical microscopy (OM) images were acquired with a Zeiss Axio Imager microscope.

Result and Discussion

We used 4.14 and 5.60 nm PbS NPs stabilized with oleic acid that can form bcc and fcc SCs, respectively.[23] While PbS NPs smaller than 3 nm adopt a spherical shape, it is known that larger PbS NPs possess (111) and (100) surface facets and that the ratio of (111) to (100) facets increases as the NP sizes increase from 3 to 15 nm, transforming NP shape from a truncated cube to an octahedron.[60-61] Our SAXS data obtained on 4.14 nm PbS NPs were fitted most accurately with the shape of a truncated octahedron when compared to other polyhedral shapes possible for PbS NPs such as a cuboctahedron or a truncated cube, indicating that the PbS NP has more (111) than (100) facets, consistent with the literature data[45, 62](see Figure S1 and Table S1). Considering surface-to-volume ratio and sphericity, the truncated octahedron and sphere are similar shapes (Table S1). As a result, good fitting of the SAXS data can be achieved with sphere model as well, (Figure S1) especially when NPs have some size polydispersity.

To initiate assembly of PbS NPs dispersed in toluene, we added non-solvents on the top of the NP toluene solutions as described in the Experimental Section. The slow interdiffusion of the layers formed by top polar non-solvent and bottom nonpolar toluene solution of PbS NPs destabilizes the PbS NPs to form SCs (Figure 1).[22] We chose three polar non-solvents: methanol, ethanol, and isopropanol. These polar solvents are miscible with toluene and are commonly used

in post-preparative purification of synthesized NPs from unreacted species and excess of surface ligands. Complete crystallization of PbS NPs with methanol and ethanol usually takes place within 1 week, while about 2 weeks are required for complete crystallization with isopropanol.

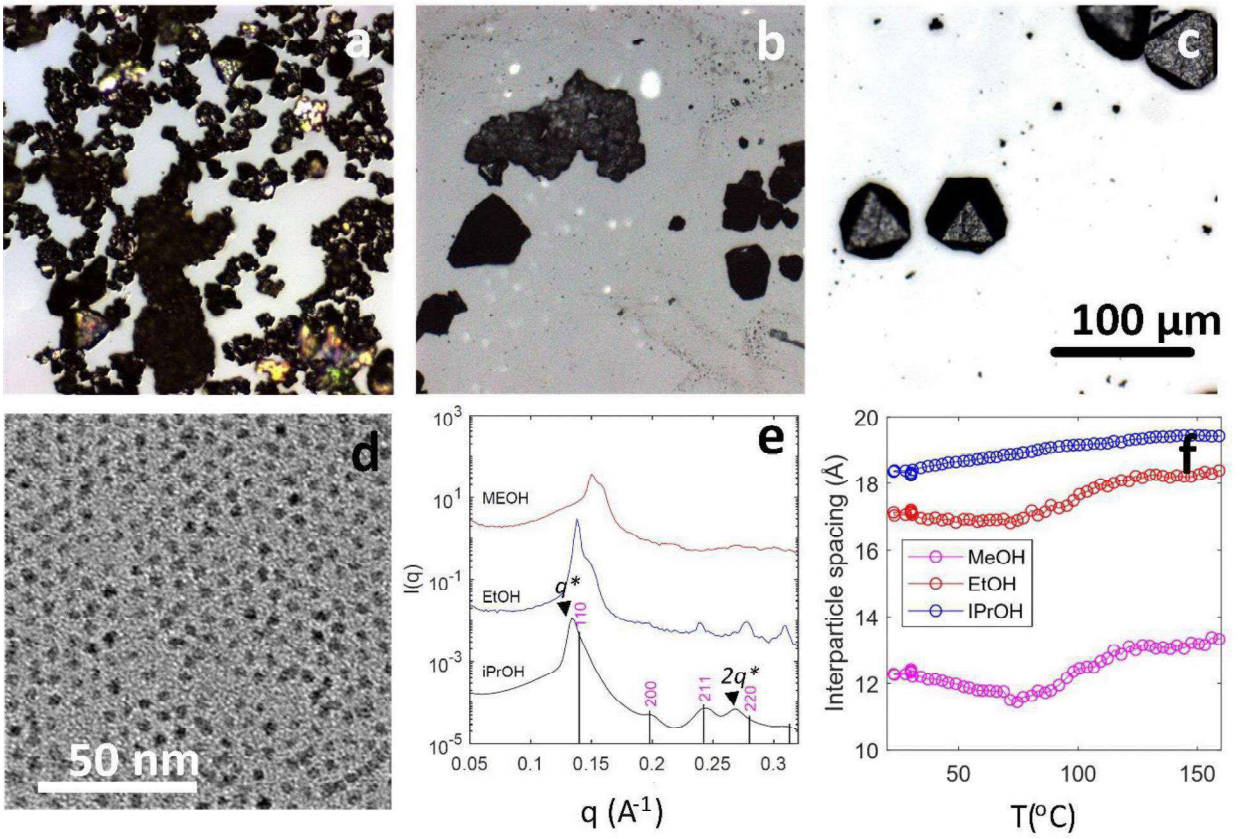

Figure 1. *Optical images of the SCs obtained by the destabilization of toluene solution of PbS NPs by methanol, ethanol, and isopropanol (a, b, and c, respectively). The scale bar in (c) applies also to (a) and (b). TEM overview of the 4.14 nm PbS NPs (d). SAXS data (e) and evolution of the interparticle spacings upon heating (f) in SCs assembled from 4.14 nm PbS NPs by different non-solvents. The peak positions in (e) are indexed with the bcc structure.*

Structural details of the SCs formed with different non-solvents. Figure 1 presents characterization results of SCs formed from 4.14 nm PbS NPs (additional information in Figures S2-S5). The size of the SCs varied with the type of non-solvent. The smallest SCs were formed with methanol, while isopropanol led to the largest SCs (Figures 1a-c). This trend was observed for all sizes of PbS NPs. While SCs from 5.60 nm PbS NPs have fcc symmetry (Figure S6), SAXS patterns acquired on SCs formed by 4.14 nm PbS NPs can be generally indexed with bcc lattice as

shown in Figure 1e with slightly shifted positions of (110) and (220) reflections and splits of their first order reflections. Note, that the shifted peaks cannot be indexed with body-centered tetragonal (bct) structure (Figure S4), which is an intermediate phase between fcc and bcc symmetry.[47] The discussion on the structural origin of the shifts will be provided below. Nonetheless, the first-order SAXS peaks appear at smaller q for SCs prepared with lower-polarity non-solvent (isopropanol), indicating a larger interparticle spacing (surface-to-surface distance) between two adjacent NPs in corresponding SCs (Figure 1e). Notably, the packing structure did not vary with the type of the non-solvents while it did vary with the PbS core size.

Figure 1f shows the temperature dependence of the interparticle spacings in the temperature range where no sintering of individual NPs is observed.[58] The interparticle spacings in all three samples generally increased with the temperature. The SCs assembled with methanol and ethanol, however, demonstrated a slight initial decrease of the interparticle spacing prior to its increase starting at 70 ^{o}C. This decrease was less pronounced for ethanol, and no decrease was observed for isopropanol. The TGA data indicated that the weight fractions of organic molecules in the SCs were around 25 %, and no systematic weight loss was observed at temperature below 70^{o}C for any of the three samples (Figure S7). Thus, the initial decrease can be associated with the structural relaxation of ligands, suggesting that ligand molecules in the as-prepared SCs have excess free volume when methanol is used as non-solvent despite the shorter interparticle spacing than those in SCs prepared with other non-solvents.

Structure analysis of the individual SCs with bcc and fcc structures. To understand the role of non-solvents, we first carefully analyzed the structure of SCs assembled with isopropanol since it allows the formation of single crystalline SCs with extended dimensions. We picked up a single SC with a needle tip and measured SAXS and WAXS with a focused x-ray beam by rotating the crystal around Z axis, changing φ angle from 0 to 180 degree (Figure S8). The measured 2D images of each SAXS and WAXS measurements were mapped into 3D reciprocal space to resolve the structural features that would be otherwise hidden in conventional SAXS analysis[63] on a randomly oriented system (Figure 2). Technical details and representative raw data are provided in the Supporting Information (Figures S8-15).

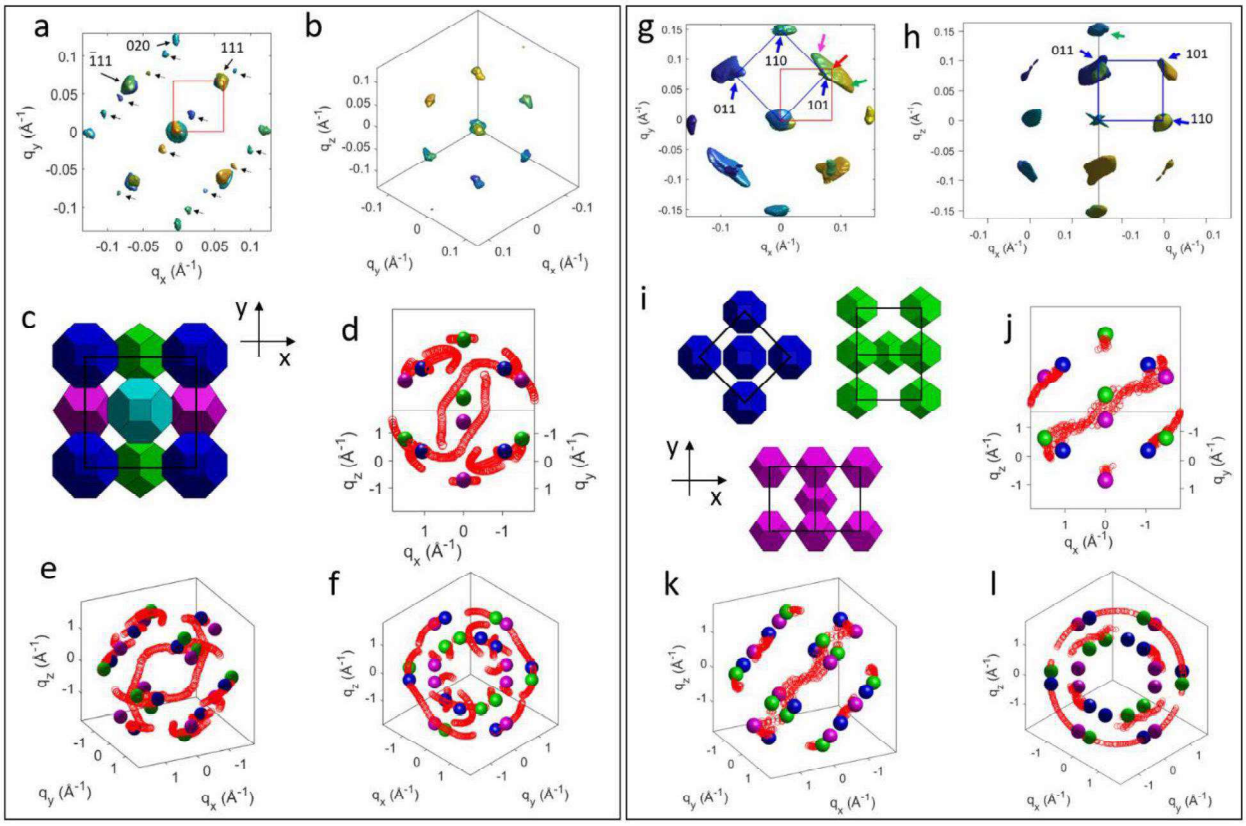

Figure 2. *SAXS and WAXS results for individual SCs assembled from 5.60 nm (a-f) and 4.14 nm (g-l) PbS NPs via destabilization of PbS NPs by isopropanol. Isosurface plot of the SAXS reciprocal space (a, b, g, and h) viewed along [001], [111], [001], and [110] directions for a, b, g, and h, respectively. The red squares in (a) and (g) depict the fcc unit cell. The blue squares in (g) and (h) depict the bcc unit cell. WAXS maps of NP(111) reflections (red open circles) for single SCs assembled from 5.60 nm and 4.14 nm NPs, (d-f) and (j-l), respectively. Color coded solid circles in (d-f) and (j-l) represent the WAXS peak position corresponding to the NP orientations shown in the fcc SC (c) and in three bcc domains in a SC (i). Color code scheme is used to describe three different orientations of individual NPs. The WAXS maps shown in (d and i), (e and k), and (f and l) viewed along [011], [121] and [1-11] directions of a cubic lattice.*

Figure 2 shows SAXS reciprocal space maps of SCs formed by 5.60 nm and 4.14 nm PbS NPs for $q < 0.15$ Å^{-1}, which include {111} and {200} reflections of the fcc SC and {110} reflections of the bcc SC. The SAXS map from a single SC formed by 5.60 nm PbS NPs confirms that it has a single-crystalline fcc structure (Figures 2a and 2b). The red square in Figure 2a represents the reciprocal space unit cell of the fcc lattice. The real-space lattice constant of this fcc SC and the interparticle spacing calculated assuming a spherical shape of NPs are 10.38 nm and 1.74 nm,

respectively. Extra reflections marked with short arrows were hidden behind other {111} reflections when viewed along [111] direction, indicating that they originate from the stacking faults along the [111] direction (Supporting Information, Movie S1).[64] When the NPs are spheres, the space group of fcc is Fm-3m with four particles in a unit cell, and their Wyckoff positions are 4a. Previous studies on the fcc periodic films formed by 11.3 nm PbS NPs upon evaporation and SCs formed by 5.5 nm NPs via the destabilization method proposed that three out of the four non-spherical NPs in the fcc unit cell possess unique orientations while the fourth NP has the same orientation as one of the three.[44-45] These characteristic orientations of NPs are shown in Figure 2c, where NP at (½, ½, 0) position, shown in cyan, has the same orientation as NPs at (0, 0, 0) position, shown in blue (Figure 2c). Since each NP is a single crystalline PbS, the orientation of NPs with respect to the lattice of a SC can be evaluated from WAXS map. For that, we calculated the positions of {111} NP reflections for three characteristic NP orientations and compared them with the measured peak positions. We denote WAXS {111} reflection from PbS NP as {111} NP. The calculated positions of {111} NP reflections are shown as color-coded solid circles (Figures 2d-2f), where color represents the NP orientation shown in Figure 2c. The [011] and [121] views of the WAXS maps reveal that the calculated positions match to some extent the measured ones shown as open circles. Each open circle is a peak position in the azimuthal line profile of {111} NP reflection measured at a given φ angle (Figure S9). When the WAXS map is viewed along the [111] direction, the measured peak positions are distributed forming more-or-less circles, suggesting a significant orientational distribution of NPs around the [111] axis of the fcc SC (Figure 2f), consistent with a recent simulation.[65] Additionally, the orientational disorder indicates that the unit cell of the PbS SC may not have fixed orientations of PbS NPs in each Wyckoff position, allowing for some degree of random permutation of the three orientations described above (for example, see Supporting Information, Movie S2).

At a first glance, the SAXS map reconstructed for a SC assembled from 4.14 nm PbS NPs (Figure 2g) looks similar to that of the fcc SC (Figure 2a). However, according to the indexing of the azimuthally averaged pattern shown in Figure 1e, the SAXS map should be the reciprocal space of the bcc lattice, where the lattice constant and interparticle spacing are 6.33 nm and 1.51 nm, respectively. The peak at the position corresponding to the fcc (111) reflection should correspond to the (101) reflection of the bcc reciprocal space unit cell shown as the blue square in Figure 2g. For better comparison with Figure 2a, we also show the fcc reciprocal space unit cell (red square).

Isosurface plots of the SAXS map reveal a few unexpected features. First, the single crystal bcc lattice should have only 12 {110} reflections; however, Figures 2g and 2h show 14 reflections (Supporting Information, Movie S3). Second, the bcc {110} reflections appearing at fcc {111} positions are much broader than others appearing at fcc {200} positions. We found that each broad reflection (Figures 2g and 2h) in fact consists of four reflections (see the pole figures in Figures 3a), corresponding to three {110} reflections from three differently-oriented bcc lattices (Figure 3c) and one {111} reflection from the fcc lattice (Figures 3b and S16a). The q values of the fcc {111} and the three bcc {110} reflections are 0.1367 $Å^{-1}$ and 0.1404 $Å^{-1}$, respectively. The interparticle spacings calculated from q values for the fcc and bcc lattices are 1.77 and 1.52 nm, respectively. Therefore, the q^* peak shown in Figure 1e is indeed {111} reflection of the fcc domain that co-exists with three bcc domains in the same SC. Figure 2i shows three bcc lattices with NP orientations allowing the highest packing density in each lattice. Interestingly, these three orientations of NPs are identical to the orientations of NPs shown in green, magenta, and blue in Figure 2c. Three NP orientations are confirmed by the WAXS maps (Figures 2j-2l). Similar to 5.60 nm NPs, 4.14 nm NPs also demonstrate some degree of random orientation around the [011] direction of the bcc lattice (Figures 2f, 2i, 3b and 3c). Note that the [011] direction in bcc lattice corresponds to the [111] direction in the fcc lattice (Figures 2a and 2g). Nevertheless, the measured {111} NP reflections presented in the WAXS maps viewed along the [011] and [121] directions match well with the peak positions expected for the three NP orientations shown in Figure 2i. Overall, the 4.14 nm NPs in the bcc SC have a higher degree of orientational order since their measured WAXS reflections are less scattered compared to those in the fcc SC formed by 5.60 nm PbS NPs (Figures 2d and 2e *vs* Figure 2j and 2k).

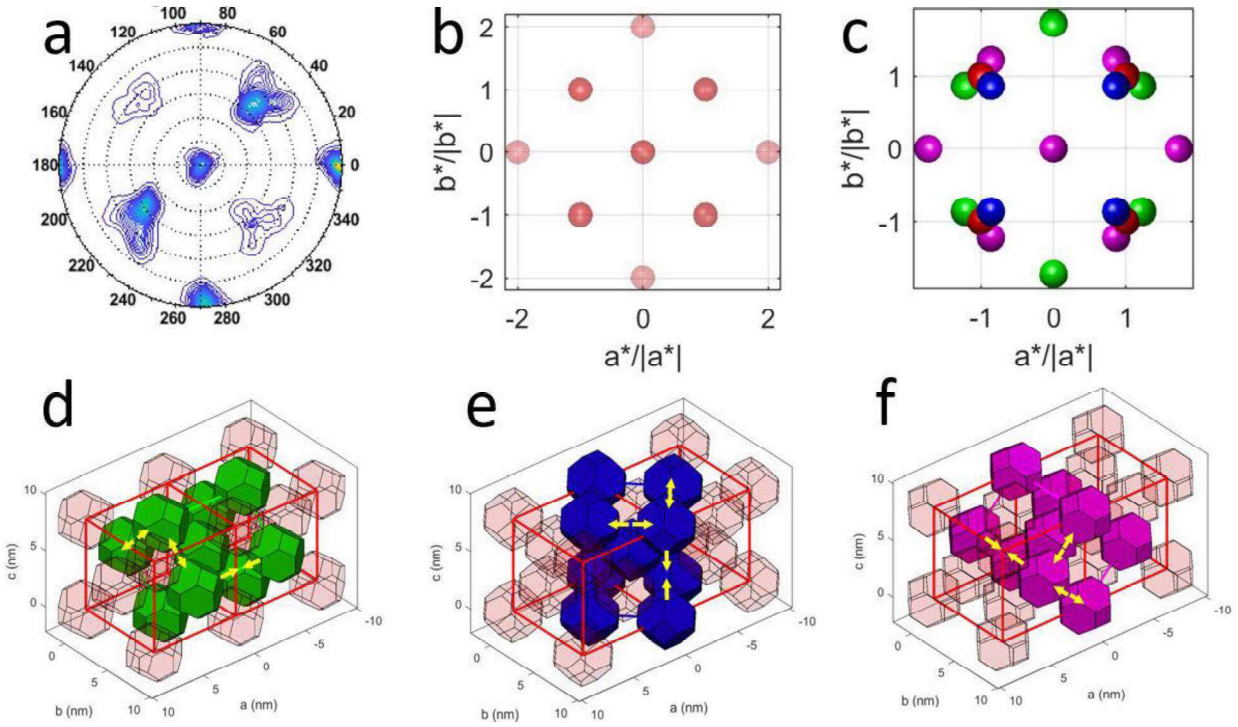

Figure 3. *Pole figure of the SC shown in Figure 2g (a). The expected positions of (111) and (002) reflections of the ideal fcc lattice, shown in (b) are surrounded by the expected position of (011) reflections of the three ideal bcc shown in Figure 2i (c). These three discrete NP orientations are shown with the green, blue and magenta truncated octahedra in the fcc lattice (d-f). Arrows in (d-f) indicate the compression directions resulting in the transformation of the fcc lattice into bcc lattices.*

Phase transformation scenario in SC. Previous studies on periodic films obtained by solvent evaporation reported the Bain transformation of fcc structures into higher-packing bcc structures.[51, 53] Consistently with this, we have observed a significantly higher packing density of three bcc domains relative to that of the fcc domain: the packing densities of 4.14 nm PbS cores for the fcc and bcc structures are 0.244 and 0.256, respectively. Our observations of the co-existence of four crystalline domains in a SC and higher packing density for the bcc domains suggest that the bcc structures originate from the fcc structure formed during the SC growth. Indeed, the three bcc domains, which are colored in green, magenta, and blue (Figures 2 and 3), can be generated by compressing the fcc lattice along a, b and c lattice axes (Figure 3a-c), respectively. We propose that the initial fcc structure has NPs with all three orientations, though

with a significant orientational degree of freedom and lack of correlation in NP orientations with respect to each other (for example, Supporting Information, Movie S2). As the fcc structure densifies to form a bcc structure, local prevalence of the NP orientations determines the type of the bcc lattice to form by controlling the local compression direction of the fcc structure. For example, in a local region where NPs with orientation shown in green are dominant (Figure 3d and Supporting Information, Movie S2), the fcc lattice would choose to shrink along the *a* axis (Figure 3d), while an area with NP orientations shown in blue as majority would prefer compression along the *c* axis (Figure 3e). This enables a higher packing bcc structure with better orientational order without a significant reorientation of NPs which, in fact, is predicted to be highly unlikely.[65]

Effect of the non-solvent on the ligands. SAXS and WAXS reciprocal space maps indicate that 5.60 nm PbS NPs assemble into the fcc lattice while 4.14 nm NPs prefer to form the bcc lattice. The orientational order of PbS NPs in the fcc lattice is not as good as that in the bcc lattice. These seem to support the notion that in the case of larger NPs, surface molecules "screen" their shape, making them behave as hard spheres preferring fcc packing. However, these packing and conformational entropy arguments cannot fully explain the non-solvent effect causing significantly different interparticle spacings (different packing density) in SCs with the same packing symmetry (Figure 1).

To study the effect of polar non-solvent on the oleic acid ligands anchored to the surface of PbS NCs, solution SAXS and SANS experiments were performed with varying amounts and types of alcohols. We used 5.60 nm PbS NCs to gain higher SANS intensities. In all experiments, toluene solutions of PbS NPs were thoroughly mixed with introduced alcohols. For all chosen alcohol concentrations, no NP sedimentation was found during the duration of our experiments (~12 h). While SAXS is only sensitive to the PbS core, SANS allows us to probe the ligand shell. To enhance the contrast of the ligand shell, deuterated toluene and alcohols were used in SANS experiments.

The SANS data were first analyzed model independently meaning no assumption of shape or morphology of NPs, allowing the construction of an appropriate model (Figures 4a and 4b). The forward scattering intensity, I(0), is proportional to the scattering contrast (the square of the scattering length density difference in the Equation S16, Supporting Information). I(0) increases

with the alcohol concentration for isopropanol but decreases for methanol (Figure 4a). Since the scattering length density of the solutions and the PbS core remain almost constant, the variation of the scattering contrast indicates solvation or de-solvation of the hydrogenated ligand shell in the deuterated solvent. The decrease in I(0) upon addition of methanol indicates the decrease of the contrast by the solvation of the shell with toluene-d8 due to its higher miscibility with oleic acid (Table 1). In contrast, the increase of I(0) upon addition of isopropanol indicates that the molecules of toluene-d8 leave the shell with increasing isopropanol content. This means that the oleic acid ligand shell was solvated when NPs were dissolved in a good solvent such as toluene. Similarly, the radius of gyration that characterizes the shell thickness decreases in the presence of methanol and increases slightly in isopropanol (Figures 4b, Figure S17).

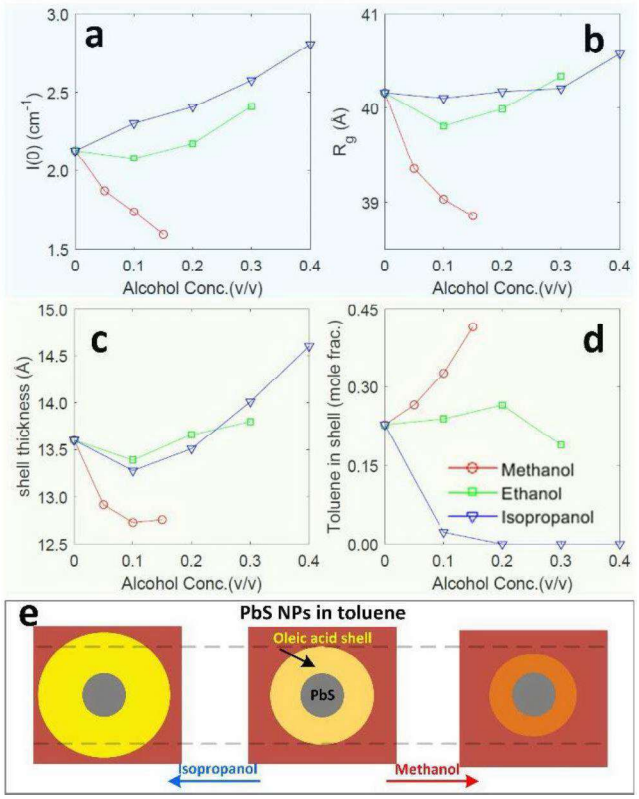

Figure 4. (*a) Model-independent analysis of SANS data obtained by extrapolation of the SANS intensity to q = 0; (b) radius of gyration (R_g) of NPs consisting of 5.60 nm PbS core and organic shell calculated from Guinier plots (log(I) vs q^2) of the SANS data; model fitting results demonstrating the ligand shell thickness (c) and mole fraction of toluene-D (d) in the ligand shell as a function of concentration of alcohols; and (e) depiction of the evolution of the ligand shell in the presence of methanol and isopropanol (the shade of orange reflects the content of the toluene-D in the ligand shell).*

In order to quantify the solvation of the NP ligand shell, we performed model fitting (Figures 4c, 4d). Based on the model independent analysis, we propose a three-layer model for PbS NPs that includes PbS core, ligand shell, and homogeneous solvent medium. Figure 4e summarizes SANS observation of the morphological evolution of the ligand shell caused by the addition of non-solvents. The ligand shell of PbS NPs dissolved in toluene-d8 is determined to be 1.35 nm thick and to contain about 23 mol % of toluene-d8. Three-layer model analysis shows that the increase of the isopropanol concentration results in the slight increase of the shell thickness (Figure 4c) and in the removal of the toluene-d8 molecules from the shell (Figure 4d), as suggested by the model independent analysis; Similar behavior was reported for Au NPs stabilized with dodecanethiol upon addition of ethanol.[66] In contrast to isopropanol, addition of methanol causes the increase of toluene-d8 concentration in the ligand shell and a decrease in the shell thickness.

Swelling and de-swelling of the ligand shell by toluene-d8 upon changing the solvent quality can be understood by considering the miscibility of corresponding substances: toluene-d8 will penetrate into the ligand shell when it has higher miscibility with the ligands than with the non-solvent. The miscibility of two substances can be estimated from the free energy of mixing (Equation 1) that reads[55]

$$\Delta G_m = RT(n_1 ln\phi_1 + n_2 ln\phi_2 + n_1\phi_2\chi_{12}) \qquad 1$$
$$\chi_{12} = V_{seg}(\delta_1 - \delta_2)^2/RT$$

where ϕ_i is a volume fraction; n_i is a mole value; δ_i is a solubility parameter of the component; χ_{12} is Flory-Huggins interaction parameters; V_{seg} is a segment volume that in our case corresponds to the volume of the solvent. The first two terms in the free energy equation represent the entropy of mixing. The third term describing the enthalpy of mixing is expressed with Flory-Huggins interaction parameter: the smaller the Flory-Huggins parameter (or the smaller the difference between the Hansen solubility parameters δ of two substances), the higher the resulting miscibility of the two substances.[67] Since the solubility parameters listed in Table 1 are not for deuterated solvent, we do not attempt a precise calculation of the Flory-Huggins interaction parameters.

However, the values of Hansen parameters for solvents are only slightly higher than that of their deuterated analogues as a result of a lower polarizability and lower vibration energy associated with shorter length of C-D as compared to C-H bonds.[68] Accordingly, the deuterated solvents are likely to have the same solubility trends, meaning that toluene-d8 mixes better with isopropanol-d8 than with methanol-d4. Toluene molecules will prefer to stay in the ligand shell when the difference between the Hansen solubility parameters of a non-solvent and toluene is larger than the difference between the toluene and oleic acid. Therefore, addition of methanol favors the higher concentrations of toluene in the ligand shell. On the other hand, introduction of the isopropanol that prefers mixing between toluene and isopropanol, leading to the extraction of toluene molecules from the ligand shell (Figure 4e).

Two possibilities are advanced to explain why de-swelling the shell increases its thickness or vice versa. First, de-swelling may cause a topological segregation of ligand molecules on the surfaces of polyhedral PbS NPs. As toluene escapes from the shell, the ligand molecules that are bound on flat faces of NPs would segregate toward the middle of each facet with stretched conformation forming a dome. While the mean shell thickness may decrease, its max value will increase. On the other hand, as toluene swells the shell, the ligands more evenly cover both the edges and faces of the polyhedral NPs in a coiled conformation, leading to a decrease in the maximum shell thickness. The second possibility is that adsorption and desorption of oleic acids on PbS in good solvents are in equilibrium, and this equilibrium may vary upon addition of non-solvent. We found that multiply washing NPs in hexane with methanol resulted in precipitates that cannot be re-dispersed any longer (Figure S18), suggesting that the equilibrium shifted toward desorption in hexane compared to in toluene. This indicates that non-solvents can make NPs unstable by removing ligands from their surfaces. Good solvent molecules, either hexane or toluene, may fill the space devoid of the ligand molecules. On the other hands, isopropanol was not as efficient in precipitating PbS NPs as methanol, suggesting that it did not desorb oleic acids but might promote adsorption of free ligand molecules. In this way, toluene in the shell can move out and the adsorbed ligand molecules will make the shell thicker. This variation of the adsorption and desorption of oleic acids is well-correlated with the solubility parameters discussed above. As toluene prefers to stay in the shell, it is more likely that desorption of ligand molecules occurs.

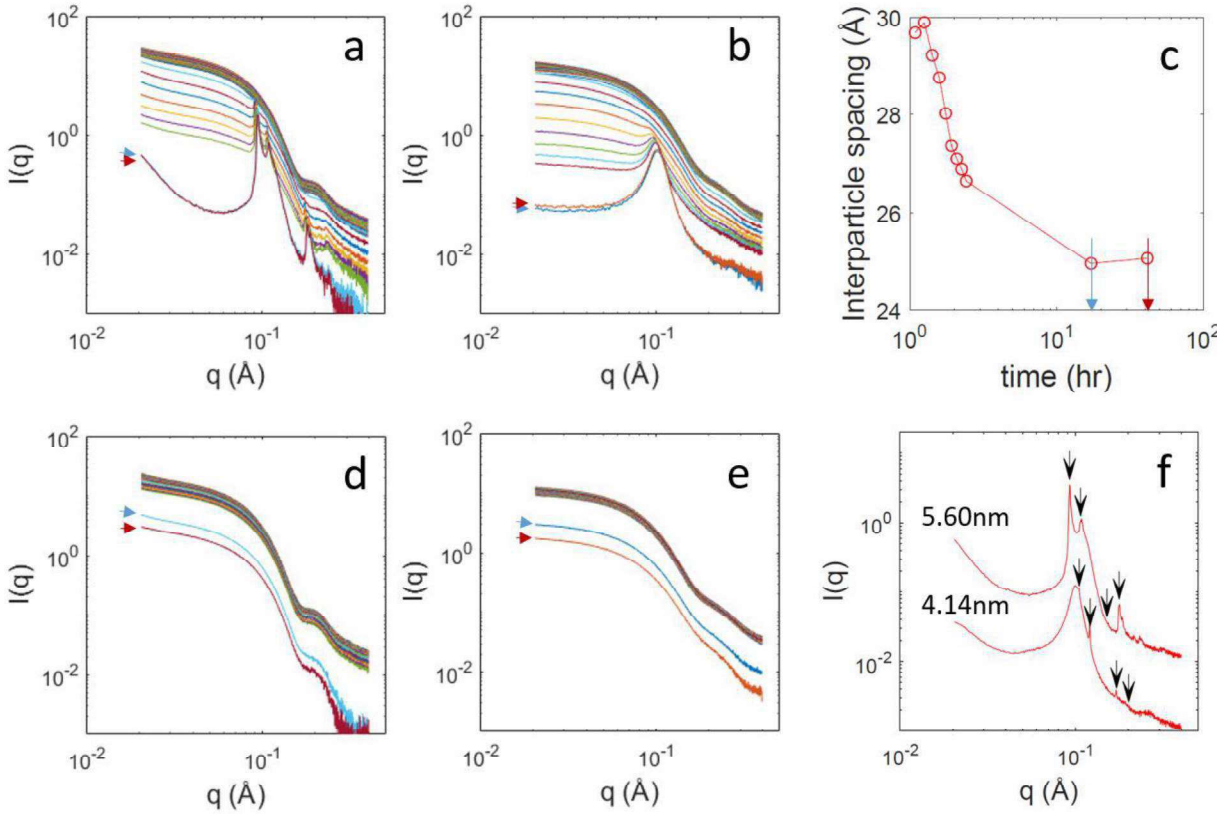
a
b
c
d
e
f
I(q)
q (Å)
Interparticle spacing (Å)
time (hr)
5.60nm
4.14nm

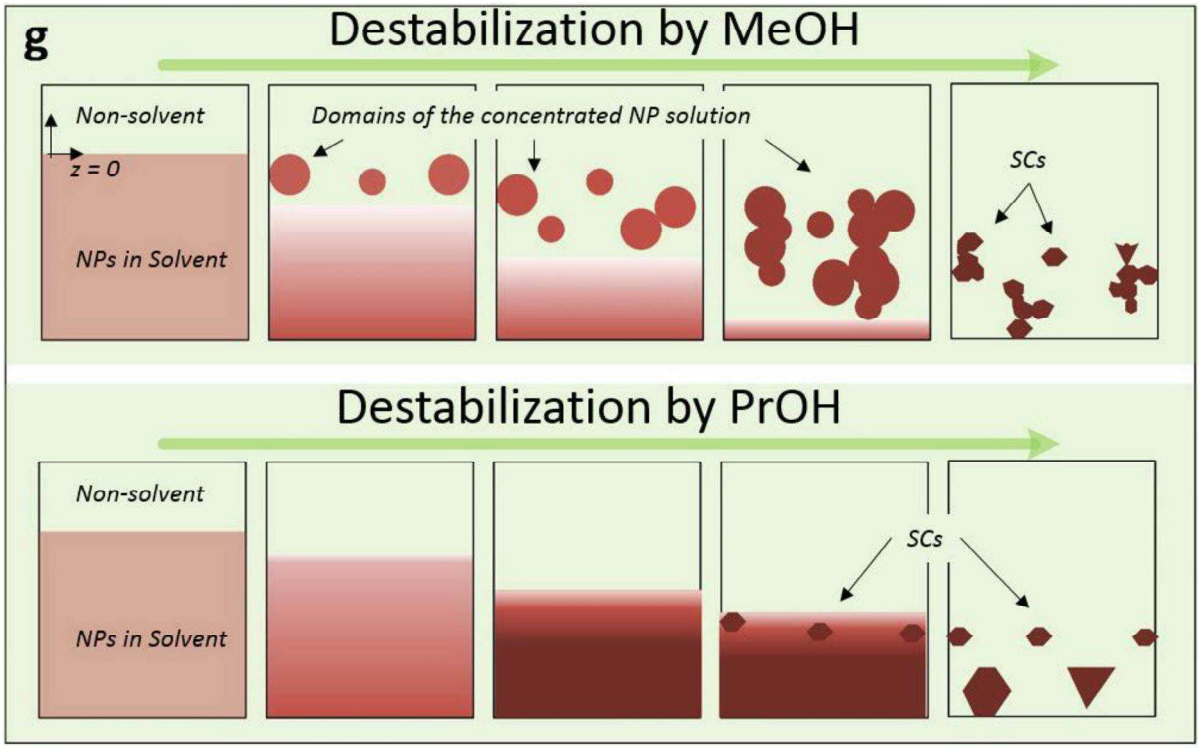
g
Destabilization by MeOH
Non-solvent
z = 0
NPs in Solvent
Domains of the concentrated NP solution
SCs
Destabilization by PrOH
Non-solvent
NPs in Solvent
SCs

Figure 5. *Summary of the in- situ SAXS results. SAXS data collected for 5.60 nm (a and d) and 4.14 nm (b and e) PbS NPs at 2mm below the original interfaces between non-solvents and toluene solutions of PbS NPs. The interfaces are at z = 0 (as defined in g), and methanol (a and b) and isopropanol (d and e) are at the top layer (z > 0). (c) Calculated interparticle spacings from data in (a). The blue and red arrows in (a, b, d, e) correspond to the times shown by the arrows in (c). (f) SAXS data measured after 40 hrs at z=-5 mm. Arrows highlight the first four reflections corresponding to the fcc lattices, with lattice constants of 11.76 and 10.37 nm for SCs assembled from 5.60 nm and 4.14 nm PbS NPs, respectively. (g) Depiction of the destabilization mechanism of the colloidal solution by non-solvents. The depth of the shade of brown represents the concentration of NPs.*

Role of non-solvent in the formation of SCs. A previous theoretical study has demonstrated that the solvation of the ligand shell determines the interactions between NPs.[54] When the ligand shells of NPs are highly solvated, neighboring NPs repel each other, while NPs with poorly-solvated ligand shells attract neighboring NPs.[54] However, in our SANS experiments, where isopropanol and NP toluene solution are mixed fast and thoroughly, de-swelling of ligand shells by isopropanol mixing did not cause strong enough NP attraction at all, while we previously showed that slow interdiffusion of the same non-solvent triggered the SC formation (Figure 1).

To understand the SC formation via slow interdiffusion of non-solvent we conducted a series of in situ SAXS experiments. In these experiments, non-solvents such as isopropanol and methanol were added on top of the toluene solutions of PbS NPs in 1.5 mm diameter quartz tubes. The bottom layer of the toluene solution of PbS NPs formed a sharp interface with the transparent, top alcohol layer. SAXS data were collected at various z positions across the interface, which is at z = 0, formed by NP toluene solution and non-solvent. When isopropanol was used as non-solvent, no NP assembly was detected in two days although the decrease of NP concentration at the initial interface was observed (Figures 5d and 5e). On the other hand, when methanol was used, 5.60 nm PbS NPs immediately formed fcc SCs at z = -2 mm, that is 2 mm below the original interface (Figure 5a); assembly of smaller 4.14 nm PbS NPs took longer. Only amorphous structures were observed at the same z position (Figure 5b), but SCs with the fcc structure were found at z = -5 mm after 40 hours (Figure 5f). We note that the SCs from 4.14 nm PbS NPs would transform to bcc structure via Bain transformation after completion of the process (Figures 1 and 2).

Figure 5c shows interparticle spacing of the fcc SCs from 5.60 nm PbS NPs determined from SAXS data acquired at z = -2 mm (Figure 5a). The initial interparticle spacing was as large as 3.0 nm (Figure 2a). We note that the similar initial interparticle spacings were observed from SCs

formed at z = -5 mm from 4.14 nm and 5.60 nm PbS NPs, which are 3.26 nm and 2.95 nm, respectively (Figure 5f). The value measured at z = -2 mm, however, quickly decreases as the non-solvent further intermixes with the toluene solution and stabilize at ~2.5 nm. We note that the initial and final values are both about 1 nm shorter than those observed for periodic films grown from the same size NPs in toluene using the solvent evaporation method.[53] Interestingly, the initial value 3 nm is about twice of the thicknesses of the NP ligand shell in pure toluene solution and toluene/methanol mixtures (Figure 4), indicating that the interparticle spacing decrease with time is driven by the removal of the toluene molecules from the NP ligand shell. The final spacing value is still ~1 nm larger than in the dried SCs, suggesting that some amount of toluene may still be trapped in the shell when methanol is used as the non-solvent—this trapped toluene may evaporate when SCs are taken out of the intermixed solution. Evaporation of the trapped solvent then creates the space for ligand relaxation upon heating, which indeed can explain the initial drops in the interparticle spacings of SCs prepared with methanol and ethanol non-solvents presented in Figure 1f. Nonetheless, as toluene molecules around NPs diffuse out by mixing with the non-solvent, NPs became locally concentrated, and repulsion between their solvated shells that refuse interdigitation caused them to pack into fcc structure similar to solvated block copolymer micelles packed into the same structure.[69]

The faster crystallization of larger 5.60 nm as compared to 4.14 nm PbS NPs can be associated with the solvation of the ligand shell. In the case of larger NPs, the smaller NP surface curvature provides a tighter arrangement of ligand molecules, facilitating the exclusion of the solvent and resulting in less-solvated ligand shells.[70-71] The more densely-packed ligands are known to drive NPs to form fcc assemblies.[65] In contrast, smaller NPs with highly solvated ligand shells provide higher net repulsive energy to neighboring NPs, slowing the NP assembly process at early stages of SC formation.

Figure 5g summarizes the mechanism of the SCs' formation. As more polar non-solvent (methanol) penetrates the colloidal NP solution, domains of highly concentrated NPs in toluene are formed. Such domains still contain large amount of the trapped solvent. Indeed, SAXS patterns collected at z = -2 mm from toluene solutions of 4.14 and 5.60 nm PbS NPs with methanol non-solvent show strong amorphous peaks at q ~0.1 $Å^{-1}$. This is indicative of the presence of localized, highly-concentrated PbS NPs. Note that in the case of 5.60 nm PbS NPs, a broad peak is hidden

under two first sharp peaks (Figures 5a and 5b). Fast intermixing of methanol with colloidal solution of NPs results in a large number of small, oversaturated domains. As the destabilization process continues, toluene is extracted from the domains into the solvent mixture, causing the assembly of NPs as evidenced by the shift of the amorphous peak positions (Figure 5b). Single-crystalline SCs grown from the domains can aggregate at later stage, resulting in the formation of irregular-shaped polycrystalline SCs, as shown in Figure 1b. On the other hand, isopropanol, which has a higher miscibility with toluene (see the Hansen parameters in Table 1) and is less immiscible with oleic acids than methanol, does not cause domain formation. No amorphous peaks corresponding to the NP-concentrated domains are observed at early stages of the crystallization process (Figures 5d, 5e). Instead, SAXS intensity gradually decreases, meaning that PbS NPs diffuse down to the toluene-rich bottom layer. Further concentration of NPs in the bottom layer initiates nucleation of the SCs, resulting in the formation of nicely-faceted, large, single-crystalline SCs (Figure 1d). Our in-situ SAXS results indicate that the use of different non-solvents allows control over the extraction of the toluene from PbS NP solution, and hence, over the oversaturation of the colloidal solution.

Table 1. *Chemical and physical parameters of solvents and ligands*

	Density (g/cm^3)	V_{molar} (cm^3/mol)	[a]SLD ($10^{-6}/A^2$)	[b]δ $(MPa)^{1/2}$
PbS	7.60	-	2.343	-
Methanol-d4	0.888	40.45	5.805	29.6
Ethanol-d6	0.892	58.4	6.098	26.5
Isopropanol-d8	0.890	76.46	5.497	23.5
Toluene-d8	0.940	105.3	5.664	18.2
Hexane	0.633	136.1	-	14.9
Oleic Acid	0.895	315.6	0.078	15.6

a. Calculated from NIST scattering length density calculator website.[72]

b. The solubility parameters are all for hydrogenated molecules.[67]

Conclusions

Using a combination of SANS, in situ SAXS, and full reciprocal-space mapping with SAXS and WAXS on individual SCs, we have identified the mechanism of the NP assembly into 3D SCs by the destabilization method. We report that the removal of the ligands is not the main driving force of the NP destabilization. In fact, the destabilization of NPs occurs because of ligand – solvent interactions that depend on the solubility of the ligands shell in a given solvent. Solubility of the ligand shell can be controlled by the addition of the non-solvent to the colloidal solution of NPs in the solvent.

Using the SANS technique, we found that the non-solvents control the degree of swelling of the ligand shell. We demonstrated that the Hansen solubility parameter of the solvent, ligands and non-solvent can be used to predict the solvation of the ligand shell that further affects the interparticle spacings in the assembled SCs. For instance, in the case of PbS NPs stabilized with oleic acids and dissolved in toluene, the ligand shell will remain solvated if the difference between the Hansen solubility parameters of an added non-solvent and toluene is larger than the difference between that of toluene and oleic acid. Therefore, the addition of methanol favors further swelling of the ligand shell by toluene while isopropanol extracts toluene molecules out from the ligand shell due to its higher miscibility with toluene. The addition of non-solvent affects the thickness of ligand shells in solution: the addition of methanol or isopropanol either decreases or increases the shell thickness, respectively. Our washing protocol test (Figure S18) and SANS results (Figure 4) indicate that in the toluene/non-solvent mixed solution, the ligand molecules tend to desorb when toluene prefers to stay in the shell and they may adsorb when toluene prefers to stay outside of the shell. We also found that the shell thicknesses in solution are directly correlated with interparticle spacing in dried SCs. SCs formed by destabilization by methanol present significantly shorter interparticle spacing than those formed by isopropanol. However, the non-solvent does not affect the packing symmetry of SCs.

We demonstrated by in situ SAXS experiments that in solution both 4.14 nm and 5.60 nm PbS NPs form SCs with fcc symmetry. Such fcc SCs have larger interparticle spacing compared to the final SCs, meaning that the ligands can “screen” the truncated octahedral shape of NPs. SAXS measurements on the dried individual single crystalline SCs formed by 4.14 nm PbS NPs revealed their transformation into a polycrystalline SCs with three unique bcc domains. This transformation

is likely to occur via a previously reported Bain transformation mechanism and is driven by the gain in the packing entropy and conformational entropy of ligands. The Bain transformation occurs in a way that the lattice compression directions for the three bcc domains observed are mutually orthogonal. On the other hand, the SCs from 5.60 nm PbS NPs retain their fcc packing symmetry upon drying. Considering the bcc structure is the densest packing structure for both NPs, we conclude that the gain in the conformational entropy of ligands plays an important role in the later stage of SC crystallization.

Our results on the mechanism of the colloidal destabilization by non-solvents can have a direct impact on the understanding of the solvent/non-solvent purification method widely used to purify synthesized NPs from the excess of organics (see for details Supporting Information, Figure S18). The experimental observation of solvent and surface-ligand interactions in the crystallization of NPs into SCs enables the comprehensive understanding of the SC formation mechanism. The ability to correlate the solvation of the NP ligand shell with the lattice parameters and SC structure opens up the opportunity to guide the assembly process not only in single component but also in multicomponent systems. Also, these results provide important insights into the assembly process induced by evaporation of the solvents from the NP solutions.

Supporting Information. Supporting information includes x-ray raw data, data analysis procedure, equations for the data analysis, TGA data, and comments on solvent/non-solvent purification protocol. The following files are available free of charge. PbS_SC_destabilization_SI.pdf (PDF); SAXS reciprocal space map of the SC from 5.60 nm PbS NPs: Movie_S1.mp4 (MP4); Real space model of the SC from 5.60 nm PbS NPs with random permutation of three NP orientations: Movie_S2.mp4 (MP4); SAXS reciprocal space map of the SC from 4.14 nm PbS NPs: Movie_S3.mp4 (MP4)

AUTHOR INFORMATION

Corresponding Author

Byeongdu Lee (blee@anl.gov) and Elena V. Shevchenko (eshevchenko@anl.gov)

Author Contributions

The manuscript was written through contributions of all authors. All authors have given approval to the final version of the manuscript.

Funding Sources

Work at the Advanced Photon Source and at the Center for Nanoscale Materials was supported by the U.S. Department of Energy, Office of Science, Office of Basic Energy Sciences, under Contract No. DE-AC0206CH-11357.

ACKNOWLEDGMENT

BL appreciates ORNL colleagues Sai Venkatesh Pingali for discussion about SANS, Panchao Yin for preliminary SANS measurements, and Kunlun Hong for kindly providing deuterated solvents. BL also appreciates Malia Wenny for proofreading. A portion of this research used resources at the High Flux Isotope Reactor, a DOE Office of Science User Facility operated by the Oak Ridge National Laboratory. Work at the Advanced Photon Source and at the Center for Nanoscale Materials was supported by the U.S. Department of Energy, Office of Science, Office of Basic Energy Sciences, under Contract No. DE-AC0206CH-11357.

ABBREVIATIONS

NP, nanoparticle; SC, supercrystal; SAXS, small angle x-ray scattering; SANS, small angle neutron scattering; WAXS, wide angle x-ray scattering; TGA, thermogravimetric analysis; OM, optical microscopy; TEM, transmission electron microscopy.

REFERENCES

1. Talapin, D. V.; Lee, J.-S.; Kovalenko, M. V.; Shevchenko, E. V., Prospects of Colloidal Nanocrystals for Electronic and Optoelectronic Applications. *Chem. Rev.* **2009,** *110* (1), 389-458.
2. Liu, W.; Halverson, J.; Tian, Y.; Tkachenko, A. V.; Gang, O., Self-organized architectures from assorted DNA-framed nanoparticles. *Nat. Chem.* **2016,** *8*, 867.
3. Lin, Q.-Y.; Mason, J. A.; Li, Z.; Zhou, W.; O'Brien, M. N.; Brown, K. A.; Jones, M. R.; Butun, S.; Lee, B.; Dravid, V. P.; Aydin, K.; Mirkin, C. A., Building superlattices from individual nanoparticles via template-confined DNA-mediated assembly. *Science* **2018,** *359* (6376), 669-672.
4. Shevchenko, E. V.; Talapin, D. V.; Kotov, N. A.; O'Brien, S.; Murray, C. B., Structural Diversity in Binary Nanoparticle Superlattices. *Nature* **2006,** *439* (7072), 55-59.
5. Nie, Z.; Petukhova, A.; Kumacheva, E., Properties and emerging applications of self-assembled structures made from inorganic nanoparticles. *Nature Nanotechnology* **2009,** *5*, 15.
6. Bishop, K. J. M.; Wilmer, C. E.; Soh, S.; Grzybowski, B. A., Nanoscale Forces and Their Uses in Self-Assembly. *Small* **2009,** *5* (14), 1600-1630.
7. Boles, M. A.; Engel, M.; Talapin, D. V., Self-Assembly of Colloidal Nanocrystals: From Intricate Structures to Functional Materials. *Chem. Rev.* **2016,** *116* (18), 11220-11289.
8. Young, K. L.; Jones, M. R.; Zhang, J.; Macfarlane, R. J.; Esquivel-Sirvent, R.; Nap, R. J.; Wu, J.; Schatz, G. C.; Lee, B.; Mirkin, C. A., Assembly of Reconfigurable One-Dimensional Colloidal Superlattices due to A Synergy of Fundamental Nanoscale Forces. *PNAS* **2012,** *109*, 2240-2245.
9. Nikoobakht, B.; El-Sayed, M. A., Evidence for Bilayer Assembly of Cationic Surfactants on the Surface of Gold Nanorods. *Langmuir* **2001,** *17* (20), 6368-6374.
10. Wu, N.; Fu, L.; Su, M.; Aslam, M.; Wong, K. C.; Dravid, V. P., Interaction of Fatty Acid Monolayers with Cobalt Nanoparticles. *Nano Lett.* **2004,** *4* (2), 383-386.
11. Jadzinsky, P. D.; Calero, G.; Ackerson, C. J.; Bushnell, D. A.; Kornberg, R. D., Structure of a Thiol Monolayer-Protected Gold Nanoparticle at 1.1 Å Resolution. *Science* **2007,** *318* (5849), 430-433.
12. Velev, O. D., Self-Assembly of Unusual Nanoparticle Crystals. *Science* **2006,** *312* (5772), 376-377.
13. Tian, C.; Cordeiro, M. A. L.; Lhermitte, J.; Xin, H. L.; Shani, L.; Liu, M.; Ma, C.; Yeshurun, Y.; DiMarzio, D.; Gang, O., Supra-Nanoparticle Functional Assemblies through Programmable Stacking. *ACS Nano* **2017,** *11* (7), 7036-7048.
14. Lin, Q.-Y.; Mason, J. A.; Li, Z.; Zhou, W.; O'Brien, M. N.; Brown, K. A.; Jones, M. R.; Butun, S.; Lee, B.; Dravid, V. P.; Aydin, K.; Mirkin, C. A., Building superlattices from

individual nanoparticles via template-confined DNA-mediated assembly. **2018,** *359* (6376), 669-672.
15. Zhu, J.; Kim, Y.; Lin, H.; Wang, S.; Mirkin, C. A., pH-Responsive Nanoparticle Superlattices with Tunable DNA Bonds. *J. Am. Chem. Soc.* **2018,** *140* (15), 5061-5064.
16. Seo, S. E.; Li, T.; Senesi, A. J.; Mirkin, C. A.; Lee, B., The Role of Repulsion in Colloidal Crystal Engineering with DNA. *J. Am. Chem. Soc.* **2017,** *139* (46), 16528-16535.
17. Murray, C. B., Kagan, C.R., Bawendi M.G. , Synthesis and characterization of monodisperse nanocrystals and close-packed nanocrystal assemblies. *Annual Review of Materials* **2000,** *30*, 545-610.
18. Shevchenko, E. V.; Talapin, D. V.; Kotov, N. A.; O'Brien, S.; Murray, C. B., Structural diversity in binary nanoparticle superlattices. *Nature* **2006,** *439*, 55.
19. Dong, A.; Chen, J.; Vora, P. M.; Kikkawa, J. M.; Murray, C. B., Binary nanocrystal superlattice membranes self-assembled at the liquid–air interface. *Nature* **2010,** *466*, 474.
20. Baker, J. L.; Widmer-Cooper, A.; Toney, M. F.; Geissler, P. L.; Alivisatos, A. P., Device-Scale Perpendicular Alignment of Colloidal Nanorods. *Nano Lett.* **2010,** *10* (1), 195-201.
21. Shevchenko, E. V.; Talapin, D. V.; Rogach, A. L.; Kornowski, A.; Haase, M.; Weller, H., Colloidal Synthesis and Self-Assembly of CoPt3 Nanocrystals. *J. Am. Chem. Soc.* **2002,** *124* (38), 11480-11485.
22. Talapin, D. V.; Shevchenko, E. V.; Kornowski, A.; Gaponik, N.; Haase, M.; Rogach, A. L.; Weller, H., A New Approach to Crystallization of CdSe Nanoparticles into Ordered Three-Dimensional Superlattices. **2001,** *13* (24), 1868-1871.
23. Podsiadlo, P.; Krylova, G.; Lee, B.; Critchley, K.; Gosztola, D. J.; Talapin, D. V.; Ashby, P. D.; Shevchenko, E. V., The Role of Order, Nanocrystal Size, and Capping Ligands in the Collective Mechanical Response of Three-Dimensional Nanocrystal Solids. *J. Am. Chem. Soc.* **2010,** *132* (26), 8953-8960.
24. Talapin, D. V.; Shevchenko, E. V.; Kornowski, A.; Gaponik, N.; Haase, M.; Rogach, A. L.; Weller, H., A New Approach to Crystallization of CdSe Nanoparticles into Ordered Three-Dimensional Superlattices. *Adv. Mater.* **2001,** *13* (24), 1868-1871.
25. Shevchenko, E.; Talapin, D.; Kornowski, A.; Wiekhorst, F.; Kötzler, J.; Haase, M.; Rogach, A.; Weller, H., Colloidal Crystals of Monodisperse FePt Nanoparticles Grown by a Three-Layer Technique of Controlled Oversaturation. *Adv. Mater.* **2002,** *14* (4), 287-290.
26. Rupich, S. M.; Shevchenko, E. V.; Bodnarchuk, M. I.; Lee, B.; Talapin, D. V., Size-Dependent Multiple Twinning in Nanocrystal Superlattices. *J. Am. Chem. Soc.* **2010,** *132* (1), 289-296.
27. Wang, Z.; Bian, K.; Nagaoka, Y.; Fan, H.; Cao, Y. C., Regulating Multiple Variables To Understand the Nucleation and Growth and Transformation of PbS Nanocrystal Superlattices. *J. Am. Chem. Soc.* **2017,** *139* (41), 14476-14482.
28. Talapin, D. V.; Shevchenko, E. V.; Bodnarchuk, M. I.; Ye, X.; Chen, J.; Murray, C. B., Quasicrystalline order in self-assembled binary nanoparticle superlattices. *Nature* **2009,** *461* (7266), 964-967.
29. Damasceno, P. F.; Engel, M.; Glotzer, S. C., Predictive Self-Assembly of Polyhedra into Complex Structures. *Science* **2012,** *337* (6093), 453-457.
30. Young, K. L.; Personick, M. L.; Engel, M.; Damasceno, P. F.; Barnaby, S. N.; Bleher, R.; Li, T.; Glotzer, S. C.; Lee, B.; Mirkin, C. A., A Directional Entropic Force Approach to Assemble Anisotropic Nanoparticles into Superlattices. *Angew. Chem. Int. Ed.* **2013,** *52* (52), 13980-13984.

31. Talapin, D. V. e. a., Seeded Growth of Highly Luminescent CdSe/CdS Nanoheterostructures with Rod and Tetrapod Morphologies. *Nano Lett.* **2007,** *7*, 2951-2959.
32. Querejeta-Fernández, A.; Hernández-Garrido, J. C.; Yang, H.; Zhou, Y.; Varela, A.; Parras, M.; Calvino-Gámez, J. J.; González-Calbet, J. M.; Green, P. F.; Kotov, N. A., Unknown Aspects of Self-Assembly of PbS Microscale Superstructures. *ACS Nano* **2012,** *6* (5), 3800-3812.
33. Xia, Y.; Nguyen, T. D.; Yang, M.; Lee, B.; Santos, A.; Podsiadlo, P.; Tang, Z.; Glotzer, S. C.; Kotov, N. A., Self-Assembly of Self-Limiting Monodisperse Supraparticles from Polydisperse Nanoparticles. *Nat. Nanotechnol.* **2011,** *6* (9), 580-587.
34. Zeng, X.; Liu, F.; Fowler, A. G.; Ungar, G.; Cseh, L.; Mehl, G. H.; Macdonald, J. E., 3D Ordered Gold Strings by Coating Nanoparticles with Mesogens. *Adv. Mater.* **2009,** *21* (17), 1746-1750.
35. Yu, C. H.; Schubert, C. P. J.; Welch, C.; Tang, B. J.; Tamba, M. G.; Mehl, G. H., Design, Synthesis, and Characterization of Mesogenic Amine-Capped Nematic Gold Nanoparticles with Surface-Enhanced Plasmonic Resonances. *J. Am. Chem. Soc.* **2012,** *134* (11), 5076-5079.
36. Macfarlane, R. J.; Lee, B.; Jones, M. R.; Harris, N.; Schatz, G. C.; Mirkin, C. A., Nanoparticle Superlattice Engineering with DNA. *Science* **2011,** *334* (6053), 204-208.
37. Huang, X.; Zhu, J.; Ge, B.; Deng, K.; Wu, X.; Xiao, T.; Jiang, T.; Quan, Z.; Cao, Y. C.; Wang, Z., Understanding Fe3O4 Nanocube Assembly with Reconstruction of a Consistent Superlattice Phase Diagram. *J. Am. Chem. Soc.* **2019,** *141* (7), 3198-3206.
38. Detlef, M. S.; Tobias, H., Superlattice self-assembly: Watching nanocrystals in action. *Europhys. Lett.* **2017,** *119* (2), 28003.
39. Wang, Z.; Schliehe, C.; Bian, K.; Dale, D.; Bassett, W. A.; Hanrath, T.; Klinke, C.; Weller, H., Correlating Superlattice Polymorphs to Internanoparticle Distance, Packing Density, and Surface Lattice in Assemblies of PbS Nanoparticles. *Nano Lett.* **2013,** *13* (3), 1303-1311.
40. Korgel, B. A.; Fitzmaurice, D., Small-Angle X-ray-Scattering Study of Silver-Nanocrystal Disorder-Order Phase Transitions. *Phys. Rev. B* **1999,** *59* (22), 14191-14201.
41. Whetten, R. L.; Shafigullin, M. N.; Khoury, J. T.; Schaaff, T. G.; Vezmar, I.; Alvarez, M. M.; Wilkinson, A., Crystal Structures of Molecular Gold Nanocrystal Arrays. *Acc. Chem. Res.* **1999,** *32* (5), 397-406.
42. McConnell, G. A.; Gast, A. P.; Huang, J. S.; Smith, S. D., Disorder-order transitions in soft sphere polymer micelles. *Phys. Rev. Lett.* **1993,** *71* (13), 2102-2105.
43. Ziherl, P.; Kamien, R. D., Maximizing Entropy by Minimizing Area: Towards a New Principle of Self-Organization. *J. Phys. Chem. B* **2001,** *105* (42), 10147-10158.
44. Li, R.; Bian, K.; Hanrath, T.; Bassett, W. A.; Wang, Z., Decoding the Superlattice and Interface Structure of Truncate PbS Nanocrystal-Assembled Supercrystal and Associated Interaction Forces. *J. Am. Chem. Soc.* **2014,** *136* (34), 12047-12055.
45. Simon, P.; Rosseeva, E.; Baburin, I. A.; Liebscher, L.; Hickey, S. G.; Cardoso-Gil, R.; Eychmüller, A.; Kniep, R.; Carrillo-Cabrera, W., PbS–Organic Mesocrystals: The Relationship between Nanocrystal Orientation and Superlattice Array. *Angew. Chem. Int. Ed.* **2012,** *51* (43), 10776-10781.
46. Bian, K.; Wang, Z.; Hanrath, T., Comparing the Structural Stability of PbS Nanocrystals Assembled in FCC and BCC Superlattice Allotropes. *J. Am. Chem. Soc.* **2012,** *134* (26), 10787-10790.
47. Choi, J. J.; Bealing, C. R.; Bian, K.; Hughes, K. J.; Zhang, W.; Smilgies, D.-M.; Hennig, R. G.; Engstrom, J. R.; Hanrath, T., Controlling Nanocrystal Superlattice Symmetry and Shape-

Anisotropic Interactions through Variable Ligand Surface Coverage. *J. Am. Chem. Soc.* **2011,** *133* (9), 3131-3138.
48. Goodfellow, B. W.; Yu, Y.; Bosoy, C. A.; Smilgies, D.-M.; Korgel, B. A., The Role of Ligand Packing Frustration in Body-Centered Cubic (bcc) Superlattices of Colloidal Nanocrystals. *J. Phys. Chem. Lett.* **2015,** *6* (13), 2406-2412.
49. Zhang, Y.; Lu, F.; van der Lelie, D.; Gang, O., Continuous Phase Transformation in Nanocube Assemblies. *Phys. Rev. Lett.* **2011,** *107* (13), 135701.
50. Weidman, M. C.; Yager, K. G.; Tisdale, W. A., Interparticle Spacing and Structural Ordering in Superlattice PbS Nanocrystal Solids Undergoing Ligand Exchange. *Chem. Mater.* **2015,** *27* (2), 474-482.
51. Bian, K.; Choi, J. J.; Kaushik, A.; Clancy, P.; Smilgies, D.-M.; Hanrath, T., Shape-Anisotropy Driven Symmetry Transformations in Nanocrystal Superlattice Polymorphs. *ACS Nano* **2011,** *5* (4), 2815-2823.
52. Quan, Z.; Wu, D.; Zhu, J.; Evers, W. H.; Boncella, J. M.; Siebbeles, L. D. A.; Wang, Z.; Navrotsky, A.; Xu, H., Energy landscape of self-assembled superlattices of PbSe nanocrystals. *PNAS* **2014,** *111* (25), 9054-9057.
53. Weidman, M. C.; Smilgies, D.-M.; Tisdale, W. A., Kinetics of the self-assembly of nanocrystal superlattices measured by real-time in situ X-ray scattering. *Nat. Mater.* **2016,** *15* (7), 775-781.
54. Kaushik, A. P.; Clancy, P., Solvent- driven symmetry of self- assembled nanocrystal superlattices—A computational study. *J. Comput. Chem.* **2013,** *34* (7), 523-532.
55. Flory, P. J., *Principles of Polymer Chemistry*. Cornell Univ. Press: Ithaca, New York, 1953.
56. Dutta, N.; Green, D., Impact of Solvent Quality on Nanoparticle Dispersion in Semidilute and Concentrated Polymer Solutions. *Langmuir* **2010,** *26* (22), 16737-16744.
57. Yang, G.; Kim, K.; Wang, W.; Chen, B.; Mattoussi, H.; Hallinan Jr., D. T., Scaling Laws for Polymer Chains Grafted onto Nanoparticles. *Macromol. Chem. Phys.* **2018,** *219* (8), 1700417.
58. Lee, B.; Podsiadlo, P.; Rupich, S.; Talapin, D. V.; Rajh, T.; Shevchenko, E. V., Comparison of Structural Behavior of Nanocrystals in Randomly Packed Films and Long-Range Ordered Superlattices by Time-Resolved Small Angle X-ray Scattering. *J. Am. Chem. Soc.* **2009,** *131* (45), 16386-16388.
59. Goodfellow, B. W.; Patel, R. N.; Panthani, M. G.; Smilgies, D.-M.; Korgel, B. A., Melting and Sintering of a Body-Centered Cubic Superlattice of PbSe Nanocrystals Followed by Small Angle X-ray Scattering. *J. Phys. Chem. C* **2011,** *115* (14), 6397-6404.
60. Cho, K. S., Talapin, D.V., Gaschler, W., Murray, C. B., Designing PbSe nanowires and nanorings through oriented attachment of nanoparticles. *J. Am. Chem. Soc.* **2005,** *127*, 7140-7147.
61. Weidman, M. C.; Smilgies, D.-M.; Tisdale, W. A., Kinetics of the self-assembly of nanocrystal superlattices measured by real-time in situ X-ray scattering. *Nature Materials* **2016,** *15*, 775.
62. Simon, P.; Bahrig, L.; Baburin, I. A.; Formanek, P.; Röder, F.; Sickmann, J.; Hickey, S. G.; Eychmüller, A.; Lichte, H.; Kniep, R.; Rosseeva, E., Interconnection of Nanoparticles within 2D Superlattices of PbS/Oleic Acid Thin Films. *Adv. Mater.* **2014,** *26* (19), 3042-3049.
63. Li, T.; Senesi, A. J.; Lee, B., Small Angle X-ray Scattering for Nanoparticle Research. *Chem. Rev.* **2016,** *116* (18), 11128–11180.

64. Byelov, D. V.; Hilhorst, J.; Leferink op Reinink, A. B. G. M.; Snigireva, I.; Snigirev, A.; Vaughan, G. B. M.; Portale, G.; Petukhov, A. V., Diffuse Scattering in Random-Stacking Hexagonal Close-Packed Crystals of Colloidal Hard Spheres. *Phase Transit.* **2010,** *83* (2), 107-114.
65. Fan, Z.; Grünwald, M., Orientational Order in Self-Assembled Nanocrystal Superlattices. *J. Am. Chem. Soc.* **2019,** *141* (5), 1980-1988.
66. Von White, G.; Mohammed, F. S.; Kitchens, C. L., Small-Angle Neutron Scattering Investigation of Gold Nanoparticle Clustering and Ligand Structure Under Antisolvent Conditions. *J. Phys. Chem. C* **2011,** *115* (38), 18397-18405.
67. Hansen, C. M., *Hansen Solubility Parameters: A User's Handbook*. second ed.; CRC Press: 2007.
68. Graessley, W. W.; Krishnamoorti, R.; Balsara, N. P.; Fetters, L. J.; Lohse, D. J.; Schulz, D. N.; Sissano, J. A., Effect of deuterium substitution on thermodynamic interactions in polymer blends. *Macromolecules* **1993,** *26* (5), 1137-1143.
69. Hanley, K. J.; Lodge, T. P.; Huang, C.-I., Phase Behavior of a Block Copolymer in Solvents of Varying Selectivity. *Macromolecules* **2000,** *33* (16), 5918-5931.
70. Von White, G.; Kitchens, C. L., Small-Angle Neutron Scattering of Silver Nanoparticles in Gas-Expanded Hexane. *J. Phys. Chem. C* **2010,** *114* (39), 16285-16291.
71. De Roo, J.; Yazdani, N.; Drijvers, E.; Lauria, A.; Maes, J.; Owen, J. S.; Van Driessche, I.; Niederberger, M.; Wood, V.; Martins, J. C.; Infante, I.; Hens, Z., Probing Solvent–Ligand Interactions in Colloidal Nanocrystals by the NMR Line Broadening. *Chem. Mater.* **2018,** *30* (15), 5485-5492.
72. Munter, A. Scattering Length Density Calculator. https://www.ncnr.nist.gov/resources/sldcalc.html (accessed 3/26).

BRIEFS. Solvent-ligand interaction for crystallization of nanoparticles.

SYNOPSIS